Research Article

Zhenhao Li, Song Yang, Xiaoning Liu, Guoqing Xiao, Hongzhan San, Yanru Zhang, Wei Wang*, and Zhibo Yang*

Grinding force model for ultrasonic assisted grinding of y-TiAl intermetallic compounds and experimental validation

https://doi.org/10.1515/rams-2023-0167 received October 17, 2023; accepted December 27, 2023

Abstract: The introduction of ultrasonic vibration in the grinding process of γ -TiAl intermetallic compounds can significantly reduce its processing difficulty. It is of great significance to understand the grinding mechanism of γ -TiAl intermetallic compounds and improve the processing efficiency by studying the mechanism of ordinary grinding of abrasive grains. Based on this, this study proposes a grinding force prediction model based on singlegrain ultrasonic assisted grinding (UAG) chip formation mechanism. First, the prediction model of grinding force is established based on the chip formation mechanism of abrasive sliding ordinary grinding and the theory of ultrasonic assisted machining, considering the plastic deformation and shear effect in the process of material processing. Second, the UAG experiment of γ -TiAl intermetallic compounds was

carried out by using diamond grinding wheel, and the unknown coefficient in the model was determined. Finally, the predicted values and experimental values of grinding force under different parameters were compared to verify the rationality of the model. It was found that the maximum deviation between the predicted value of tangential force and the actual value is 23%, and the maximum deviation between the predicted value of normal force and the actual value is 21.7%. In addition, by changing the relevant parameters, the model can predict the grinding force of different metal materials under different processing parameters, which is helpful for optimizing the UAG parameters and improving the processing efficiency.

Keywords: γ-TiAl intermetallic compounds, prediction model, mechanism research, ultrasonic assisted grinding, comparative verification

average undeformed chip thickness

* Corresponding author: Wei Wang, School of Emergency Management, Henan Polytechnic University, Jiaozuo, 454000, China, e-mail: wangwei@hpu.edu.cn

Zhenhao Li: School of Mechanical and Power Engineering, Henan Polytechnic University, Jiaozuo, 454000, China,

e-mail: zhenhao1128@126.com

Song Yang: School of Software, Henan Polytechnic University, Jiaozuo, 454000, China, e-mail: 2682139520@qq.com

Xiaoning Liu: School of Mechanical and Power Engineering, Henan Polytechnic University, Jiaozuo, 454000, China,

e-mail: 1143460674@qq.com

Guoqing Xiao: School of Mechanical and Power Engineering, Henan Polytechnic University, Jiaozuo, 454000, China,

e-mail: xgq77923@163.com

Hongzhan San: School of Materials Science and Engineering, Henan Polytechnic University, Jiaozuo, 454000, China,

e-mail: Hongshansan@hpu.edu.cn

Yanru Zhang: School of Mechanical and Power Engineering, Henan Polytechnic University, Jiaozuo, 454000, China, e-mail: zhangyanru@hpu.edu.cn

Nomenclature

 $a_{\rm c}$

grinding depth
ultrasonic amplitudes
grinding width
coefficients related to the physical
properties of the workpiece material
effective contact area of the work-
piece-abrasive
component force of F in any direction
correlation coefficients
chip formation force
normal chip formation force
during UAG
normal plowing force during UAG
normal sliding force between a single
abrasive particle and the workpiece
normal sliding force during UAG
plowing force

^{*} Corresponding author: Zhibo Yang, Institute of Mechanical and Electrical Engineering, Hebi Polytechnic, Hebi, 458030, China, e-mail: yangzhibo@hpu.edu.cn

$F_{ m p}$	grinding force per unit area in the	Γ
	plowing stage	d_{s}
$F_{ m sl}$	sliding force	$\xi_{ m sl}$
$F_{\rm t,ch}$	tangential chip formation force	
	during UAG	$\xi_{ m pl}$
$F_{ m t,pg}$	tangential plowing force during UAG	•
$F_{\rm t,sl}$	tangential sliding force during UAG	$\xi_{ m ch}$
g	correlation coefficient	
k_1 , k_3 , k_4 , and k_5	correlations coefficient	ς
k_2 , k_6 , k_7 , k_8 ,	constants	
and k_9		ψ
$l_{ m g}$	busbar of the contact zone between	
	the grain and the workpiece	α , β , and γ
l_{s}	grinding arc length	и
$N_{ m dt}'$	distribution density of dynamic	
	effective abrasive particles	τ
$N_{ m dt}$	total number of dynamic effective	\mathcal{V}'
	abrasive grains on the grinding wheel	γ
	surface	ϕ
$N_{ m d,ch}$	dynamic effective abrasive grain	Δs
	counts in the chip formation stage	γ_0'
$N_{ m d,pl}$	dynamic effective abrasive grain	- 0
•	counts in the plowing stage	
$N_{ m d,sl}$	dynamic effective abrasive grain	
	counts in sliding stage	1 Intro
P_0	constant	
$ar{P}$	average contact pressure of a single	γ-TiAl interr
	abrasive particle-workpiece	density, higl
r	radius of the S-region	good high-te
Š	effective contact area of a single	pounds can
	abrasive particle-workpiece	only about
T	deformation temperature	sidered to b
UAG	ultrasonic assisted grinding	nickel-based
u_{ch}	grinding specific energy of single	prospect in
	abrasive grain in chip formation	and automo
	stage	pounds are
$u_{\mathrm{ch,st}}$	static grinding specific energy in chip	their high st
	formation stage	Ultrasoi
$u_{\mathrm{ch,dy}}$	dynamic grinding specific energy in	mance hybr
	chip formation stage	processing i
$v_{\rm s}$	grinding wheel speed	with ultrasc
$v_{ m W}$	workpiece speed	realize the
$\mu_{ m sl}$	friction coefficient of abrasive-work-	materials su
	piece contact surface in sliding stage	UAG can ef
$\mu_{ m pl}$	friction coefficient of abrasive-work-	temperature
	piece contact surface in plowing stage	improveme
$\mu_{ m ch}$	friction coefficient of abrasive-work-	[12–14]. The
	piece contact surface in the chip for-	et al. [15] ca
	mation stage	tional filing
Δ	deviation between the radius of the	quality, and
_		1 ,

grinding wheel and the curvature

radius of the grinding path

Γ	grinding area
d_{s}	radius of the grinding wheel
$\xi_{ m sl}$	proportion of dynamic effective
	grains in the sliding stage
$\xi_{ m pl}$	proportion of dynamic effective
	grains in the plowing stage
$\xi_{ m ch}$	proportion of dynamic effective
	grains in the chip formation stage
ς	ratio of grinding wheel speed to
	vibration speed
ψ	angle between any direction and the
	workpiece feed direction
α , β , and γ	constants
и	energy consumed to remove the unit
	volume of material
τ	shear flow stress
γ'	shear strain rate
γ	shear strain
ϕ	shear angle
Δs	thickness of shear band
$\mathcal{V}_0^{'}$	constant

1 Introduction

y-TiAl intermetallic compounds have the advantages of low density, high specific strength, strong creep resistance, and good high-temperature stability [1]. γ -TiAl intermetallic compounds can still work normally at 900°C, and its density is only about 50% of the nickel-based alloy. It is widely considered to be a high-temperature alloy that can replace the nickel-based alloy in the future, and has a good application prospect in high-end manufacturing fields such as aviation and automobile [2,3]. However, γ -TiAl intermetallic compounds are typical difficult-to-machine materials due to their high strength, poor plasticity, and high hardness [4,5].

Ultrasonic assisted grinding (UAG) is a high-performance hybrid machining technology [6–8]. As an advanced processing method, UAG combines conventional grinding with ultrasonic vibration, which is an effective method to realize the precision machining of difficult-to-machine materials such as titanium alloy [9–11]. At the same time, UAG can effectively reduce the grinding force, grinding temperature, and surface roughness with the significant improvement of the surface residual compressive stress [12–14]. Therefore, UAG has been widely studied. Wang et al. [15] carried out ultrasonic assisted filing and traditional filing experiments, comparing the force, surface quality, and surface roughness generated during the processing of the two. The results showed that the processing effect is better after applying ultrasonic vibration. Dong

et al. [16] designed a single-factor experiment to study the effect of ultrasonic vibration on the grinding edge size of deep holes. The results show that the application of ultrasonic vibration improves the quality of the hole. It can be found that the applied ultrasonic vibration provides better machining results compared to conventional machining.

As an important factor to evaluate the machining effect, grinding force plays an important role in the study of the grinding mechanism [17-20]. Studies have shown that the magnitude of the grinding force directly affects the machining accuracy of the workpiece and the quality of the machined surface [21–23]. Therefore, scholars studied the grinding force when machining y-TiAl intermetallic compounds. Studies have shown that there are some differences in grinding force when using different types of grinding wheels to carry out grinding experiments, which is mainly due to the different levels of wear of the grinding wheel during the grinding process [24,25]. Xi et al. used different kinds of grinding wheels to grind y-TiAl intermetallic compounds and found that the diamond grinding wheel has the best grinding effect, followed by the CBN grinding wheel [26,27]. In addition, Hood et al. [28,29] have reported the grinding results of y-TiAl intermetallic compounds: when using SiC grinding wheel to grind the workpiece surface, the cutting depth is the most important factor affecting the grinding force, rather than the grinding wheel size, grinding wheel grade, and grinding wheel structure. Moreover, under the same grinding conditions, the normal force, size, and change trend of the workpiece are the same as those of Ti-6Al-4V alloy, while the tangential force is only about half of that of Ti-6Al-4V alloy. Chen et al. [30] used the grey correlation analysis method to obtain the influencing factors in the grinding process of y-TiAl intermetallic compounds. It was found that the grinding depth has the greatest influence on the normal grinding force and grinding temperature of y-TiAl intermetallic compounds, while the wheel speed has the greatest influence on the tangential grinding force. In addition, Chen et al. also obtained the optimal parameter combination for y-TiAl intermetallic compounds grinding: $v_s = 90 \text{ m} \cdot \text{s}^{-1}$, $v_w = 0.5 \text{ m} \cdot \text{min}^{-1}$, $a_q = 0.1 \text{ mm}$.

Furthermore, the establishment of grinding force prediction model is of great significance for optimizing grinding process parameters and improving processing efficiency and quality. For the effective help for the study of grinding process, scholars have conducted a lot of research on grinding force prediction model [31,32]. Generally speaking, the abrasive grain goes through three stages from cutting in to cutting out, and the grinding force can be considered as the sum of the grinding force of the abrasive grain at different stages in the grinding area. On

this basis, researchers have proposed some more accurate grinding force prediction models based on the mechanism of abrasive scratches. Through experimental analysis, Hou and Komanduri [33] found that the critical cutting depth of the plow and chip formation transition is related to the abrasive particle size, which can be approximately expressed as 0.025 times the abrasive particle size. Durgumahanti et al. [34] proposed a method for calculating the total normal force and tangential force of the three stages of sliding, plowing, and chip formation by using the grinding process parameters, and determined the undetermined coefficients in the expression through experiments. The results showed that the predicted values obtained by this method are in good agreement with the experimental values. Based on Hertz's contact theory, Jiang et al. [35] further determined the critical depth of friction and tillage transition. Li et al. [36] proposed a new method to predict the grinding force, which provides detailed information, including three parts: sliding, plowing, and chip formation. In addition, Li proposed a new strategy to determine the grain-workpiece interaction at each grinding moment and a novel grinding kinematics derivation method considering different grain protrusions. However, the above methods for determining the critical cutting depth are derived based on simplifying the shape of the abrasive particles, so there are some limitations.

Besides, the critical cutting depth is a quantity related to the material properties, and the results of theoretical derivation are not accurate. Based on the research results of Li et al., Zhang et al. [37] introduced the plastic accumulation theory and cutting efficiency into the single-grain scratch test, which determined the critical cutting depth of plowing and cutting transition, and optimized the grinding force model. From the three stages of metal material removal, Li et al. [38] established a grinding force model for nickel-based high-temperature alloy FGH96 in combination with the theoretical derivation and empirical formulas, taking into account the contact sliding between abrasive grains and the workpiece, the plastic deformation of the material at the plowing stage, and the shear strain effect of the abrasive chip formation on the grinding process. The results showed that the experimental values match the predicted values quite well. The errors of tangential grinding force and normal grinding force are 9.8 and 13.6%, respectively. It is found that the sliding force generated in the sliding friction stage is the main source of grinding force. Ma et al. [39] divided the contact area into micro-elements and established a dynamic grinding force model for face gear grinding. The results showed that the agreement degree of prediction values and experimental values is high, and the errors of normal force and tangential force are within ±0.3 and ±0.1 N, respectively. Based on

Benkai's research, Yi et al. [40] established a calculation model of grinding force in the grinding process of a straight groove structure grinding wheel. Through the comparison of the results, it is found that the theoretical value is in good agreement with the experimental value, and the maximum calculation errors of tangential grinding force and normal grinding force are 14.5 and 11.8%, respectively. In addition, when the intermittent ratio of the structured grinding wheel is constant, the groove width has little effect on the grinding force. When the groove width is constant, the intermittent ratio has a great influence on the grinding force. With the increase in the intermittent ratio, the grinding force decreases obviously. Based on the double mechanism of the grinding effect of the rake face and the cutting effect of the cutter surface, Duan et al. established the instantaneous milling force model of the integral end mill under the condition of dry nanofluid micro-lubrication. The average absolute error of the force in the x, y, and z directions of the prediction model is 13.3, 2.3, and 7.6%, respectively [41]. Liu proposed an improved grinding force model based on the geometric characteristics of random grains, and verified the model by TC4 dry grinding test. The experimental results showed that the numerical calculation and experimental measurement results are in good agreement under different processing parameters, and the minimum error value is only 1.2022%, which indicates that the calculation accuracy of the grinding force model meets the requirements and is feasible [42,43].

In addition, the researchers predicted the UAG force. Based on the different characteristics of materials, Abdelkawy et al. [44] studied the change in UAG force based on plasticbrittle transition. To explore the influence of UAG parameters on grinding force, Lei et al. [45] established a dynamic model of instantaneous grinding force in UAG, analyzed the wear forms of grinding wheel abrasive grains through experiments, and discussed the reasons for the formation of different wear forms. Based on the study of a single abrasive grain, Zhang et al. [46] proposed an analytical model of grinding force considering the ductile-brittle transition, and established a final model of the number of active abrasive grains in the cutting area, and verified the rationality of the model through experiments. Based on the law of conservation of pulse, Vickers hardness theory, and indentation fracture mechanics theory, Liu et al. [47] established a prediction model of ZrO2 ceramic UAG force considering plastic removal and brittle fracture material removal mechanism. The correctness of the theoretical model was verified by experiments, and the average error between the theoretical value and the experimental value was 22.87%. In addition, Liu et al. also found that the rotary UAG force can be reduced by up to 66.76%. Lu et al. [48] established a key undeformed

cutting depth prediction model for elliptical vibration assisted cutting of BK7 optical glass. By comparing the experimental results with the predicted results, the average error between the two is only 12%, which verifies the accuracy of the model.

There is no research on the application of chip formation mechanism based on single abrasive grain grinding in ultrasonic assisted machining. Therefore, based on the combination of single abrasive grain grinding chip formation mechanism and ultrasonic assisted machining theory, this study proposes a single abrasive grain UAG chip formation mechanism, and establishes a grinding force prediction model based on this mechanism. The model considers three key factors: the friction between the abrasive and the workpiece, the plastic deformation of the material during the abrasive plowing process, and the shear strain effect of the material during the chip formation process. By modifying the relevant parameters in the ultrasonic assisted grinding prediction force model, the ultrasonic assisted grinding force of other workpieces can be predicted. At the same time, the rationality of the model was verified by the UAG experiment of y-TiAl intermetallic compounds with diamond grinding wheel.

2 Establishment of predictive force model for UAG

The grinding thickness of a single abrasive grain formed by the interference between any abrasive grain on the grinding wheel and the workpiece gradually increases, and the change in the grinding thickness leads to the change in the interaction mechanism between the single abrasive grain and the workpiece material. Therefore, the chip formation mechanism based on single abrasive grain grinding is formed. The application of ultrasonic vibration during the grinding process changes the trajectory of the abrasive particles, The chip formation mechanism based on single abrasive UAG is formed.

Since the grinding force in the grinding process is the resultant force of the grinding force generated by the abrasive grains participating in the grinding of the whole grinding wheel surface, it is necessary to study the grinding force of a single abrasive grain for studying the grinding force in the whole grinding process. Studies have shown that grain shape during grinding has an important effect on the chip formation mechanism and grinding force [20]. In this study, a conical equivalent abrasive grain model with a top angle of 2θ , is used to better explain the mechanism of grinding force generation.

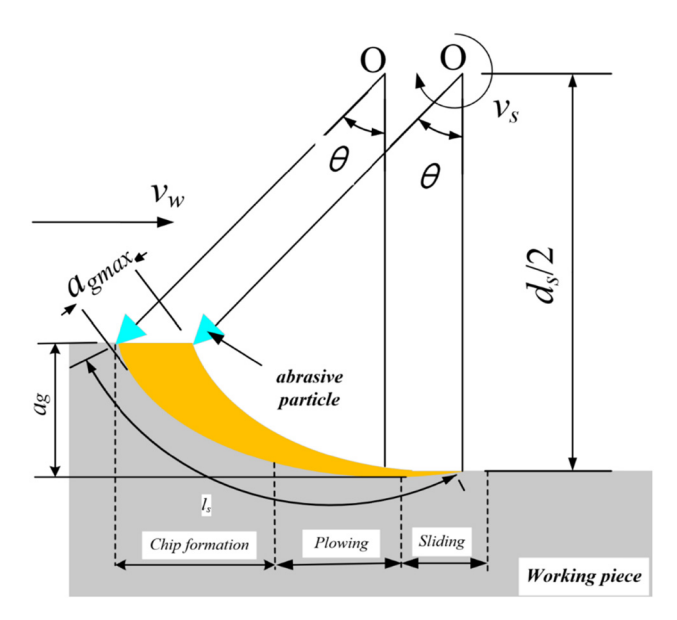


Figure 1: Abrasive particle trajectory diagram.

During UAG, the trajectory of abrasive grain movement is shown in Figure 1. As can be seen from Figure 1, the ultrasound-assisted grinding process has three stages: sliding, plowing, and chip formation. Therefore, the grinding force during the grinding process can be regarded as the superposition of the grinding force in the three stages of sliding friction, plowing, and chip formation:

$$F = F_{\rm sl} + F_{\rm pl} + F_{\rm ch},$$
 (1)

where F_{sl} is the sliding force, F_{pl} is the plowing force, and F_{ch} is the chip formation force.

The calculation of tangential grinding force and normal grinding force is shown in formula (2).

$$\begin{cases} F_{t} = F_{t,sl} + F_{t,pl} + F_{t,ch} \\ F_{n} = F_{n,sl} + F_{n,pl} + F_{n,ch}. \end{cases}$$
 (2)

Among

$$\begin{bmatrix} F_{t,sl} \\ F_{t,pl} \\ F_{t,ch} \end{bmatrix} = \begin{bmatrix} F_{n,sl} \\ F_{n,pl} \\ F_{n,ch} \end{bmatrix} (\mu_{sl} \quad \mu_{pl} \quad \mu_{ch}), \tag{3}$$

where $\mu_{\rm sl}$, $\mu_{\rm pl}$, and $\mu_{\rm ch}$ are the friction coefficients of the abrasive-workpiece contact surface at different stages, respectively.

2.1 Sliding force

In the sliding stage, the workpiece only undergoes elastic deformation. The grinding edge does not play a grinding role, only sliding on the surface of the workpiece. Therefore, the sliding force between the workpiece and the abrasive particles can be solved by the friction relationship between the two.

In the sliding stage, the normal force between the abrasive particles and the workpiece changes with the contact area between them. Therefore, the normal sliding force between a single abrasive particle and the workpiece is

$$F'_{\text{n sl}} = \bar{P} \cdot \bar{S},\tag{4}$$

where \bar{P} is the average contact pressure of a single abrasive particle-workpiece and \bar{S} is the effective contact area of a single abrasive particle-workpiece.

In the geometric dynamics analysis of abrasive grains, the parabolic function is usually used to approximately replace the grinding path. The deviation between the radius of the grinding wheel and the curvature radius of the grinding path is [49]

$$\Delta = \pm \frac{4v_{\rm w}}{v_{\rm s}d_{\rm s}}. (5)$$

There is a certain linear relationship between \bar{P} and Δ , which is given by

$$\bar{P} = P_0 \Delta = \pm \frac{4P_0 \nu_{\rm w}}{\nu_{\rm s} d_{\rm s}},\tag{6}$$

where P_0 is a constant, which can be obtained by experiments.

 $N'_{
m dt}$ is defined as the distribution density of dynamic effective abrasive particles on the surface of grinding wheel. Therefore, the total number of dynamic effective abrasive grains on the grinding wheel surface is:

$$N_{\rm dt} = N'_{\rm dt}\Gamma = N'_{\rm dt}l_{\rm S}b = N'_{\rm dt}(a_{\rm p}d_{\rm S})^{\frac{1}{2}}b, \tag{7}$$

where Γ is the area of the grinding area, $l_{\rm s}$ is the grinding arc length, b is the grinding width, $a_{\rm p}$ is the grinding depth, and $d_{\rm s}$ is the radius of the grinding wheel.

According to the research, at different stages of grinding wheel grinding, the proportion of dynamic effective abrasive grains involved in grinding is different. It is assumed that the proportions of dynamic effective grains in the sliding, plowing, and chip formation processes are $\xi_{\rm sl}$, $\xi_{\rm pl}$, and $\xi_{\rm ch}$, respectively. Then, the number of abrasive grains corresponding to three stages is as follows:

$$\begin{bmatrix} N_{\rm d,sl} \\ N_{\rm d,pl} \\ N_{\rm d,ch} \end{bmatrix} = N_{\rm dt} \begin{bmatrix} \xi_{\rm sl} \\ \xi_{\rm pl} \\ \xi_{\rm ch} \end{bmatrix}, \tag{8}$$

where $N_{d,sl}$, $N_{d,pl}$, and $N_{d,ch}$ are the dynamic effective abrasive grain counts for sliding, plowing, and chip formation, respectively.

Combining Eqs. (4), (6), and (7) yields

$$F_{\rm n,sl} = N_{\rm d,sl} \cdot F'_{\rm n,sl} = N_{\rm d,sl} \cdot \bar{P} \cdot \bar{S} = N_{\rm d,sl} \frac{4P_0 v_{\rm w}}{v_{\rm s} d_{\rm s}} \bar{S}.$$
 (9)

Let $k_1 = 4P_0\bar{S}N'_{\rm dt}\xi_{\rm sl}$, then

$$F_{\text{n,sl}} = k_1 \frac{N_{\text{dt}} \xi_{\text{sl}} \nu_{\text{w}} b}{\nu_{\text{s}} d_{\text{s}}} = k_1 \frac{a_{\text{p}}^{0.5} \nu_{\text{w}} b}{\nu_{\text{s}} d_{\text{s}}^{0.5}}.$$
 (10)

According to Li *et al.*, the dynamic friction coefficient between the abrasive grain workpiece during UAG is [50]

$$\mu_{\rm sl} = \frac{2}{\pi} \left[\frac{C_1 \bar{S}}{F_{\rm n,sl}} + C_2 \right] \frac{(\varsigma + 1)\varsigma}{\sqrt{\varsigma^2 + 1}} k_2, \tag{11}$$

where k_2 is a complete elliptic integral of the first type and is constant.

Therefore, the tangential sliding force during UAG is

$$F_{t,sl} = \mu_{sl} F_{n,sl} = k_{l} \frac{a_{p}^{0.5} v_{w} b}{v_{s} d_{s}^{0.5}} \frac{1}{\pi} \left[\frac{C_{1} \overline{S}}{F_{n,sl}} + C_{2} \right] \frac{2(\varsigma + 1)\varsigma}{\sqrt{\varsigma^{2} + 1}} k_{2}$$

$$= \frac{2k_{l} k_{2}}{\pi} \frac{a_{p}^{0.5} v_{w} b}{v_{s} d_{s}^{0.5}} \left[\frac{C_{1} \overline{S}}{F_{n,sl}} + C_{2} \right] \frac{(\varsigma + 1)\varsigma}{\sqrt{\varsigma^{2} + 1}}$$

$$= k_{3} \frac{a_{p}^{0.5} v_{w} b}{v_{s} d_{s}^{0.5}} \left[\frac{C_{1} \overline{S}}{F_{n,sl}} + C_{2} \right] \frac{v_{s} + 2\pi f A}{\sqrt{(2\pi f A)^{2} + v_{s}^{2}}}.$$
(12)

Among them, $k_3 = 2\pi k_1 k_2$.

2.2 Plowing force

The grinding force per unit area is solved by the relationship between the force per unit area between the abrasive particles and the workpiece and the component force in any direction. The grinding force per unit area is integrated, and then the complete force between the abrasive grain and the workpiece in the plowing stage is obtained.

According to Zhang *et al.* [37], the plowing force is mainly generated by the plastic flow of the materials. Therefore, the grinding force per unit area is related to the grinding parameters (such as grinding wheel speed, workpiece feed speed, and cutting depth) and certain mechanical properties of the material (such as elastic modulus and yield strength). Figure 2 shows a schematic diagram of the plowing force.

Figure 2(a) shows the relationship between the grinding force F_p per unit area and its component force dF_x in any direction. Figure 2(b) shows a schematic diagram of the plowing force of a single abrasive grain perpendicular to the conical surface.

According to Figure 2(c), the expression of force dF_x can be obtained as follows:

$$dF_x = F_0 \cos \theta \cos \psi dA, \tag{13}$$

$$dA = \frac{1}{2}rl_{g}d\psi = a_{g}^{2}\frac{\tan\theta}{\cos\theta}d\psi.$$
 (14)

Substituting formula (14) in formula (13), we can obtain

$$dF_x = F_p \cos \theta \cos \psi dA = \frac{1}{2} F_p a_g^2 \tan \theta \cos \psi d\psi, \quad (15)$$

where dA is the effective contact area of the workpiece-abrasive, r is the radius of the S region, $l_{\rm g}$ is the busbar of the contact zone between the grain and the workpiece, and ψ is the angle between any direction and the workpiece feed direction.

Therefore, the normal plowing force and tangential plowing force acting on a single abrasive grain are

$$\begin{cases} dF_{t,pg} = dF_x \cos\theta \cos\psi = \frac{1}{2}F_p a_g^2 \sin\theta \cos^2\psi d\psi \\ dF_{n,pg} = dF_x \sin\theta = \frac{F_p a_g^2 \sin^2\theta \cos\psi}{2\cos\theta} d\psi. \end{cases}$$
(16)

The integral can be obtained as follows:

$$\begin{cases} F'_{t,pg} = \int_{-\frac{\pi}{2}}^{\frac{\pi}{2}} \frac{1}{2} F_p a_g^2 \sin \theta \cos^2 \psi d\psi = \frac{\pi}{4} F_p a_g^2 \sin \theta \\ F'_{n,pg} = \int_{-\frac{\pi}{2}}^{\frac{\pi}{2}} \frac{F_p a_g^2 \sin^2 \theta \cos \psi}{2 \cos \theta} d\psi = \frac{F_p a_g^2 \sin^2 \theta}{\cos \theta}. \end{cases}$$
(17)

According to the experimental results, the relationship between $F_p a_g^2$ and v_w , v_s , a_p can be established [38].

$$F_{\rm p}a_{\rm g}^2 = C_3 \left(\frac{v_{\rm w}}{v_{\rm s}}\right)^{\alpha} a_{\rm p}^{\beta} d_{\rm s}^{\gamma}. \tag{18}$$

Therefore,

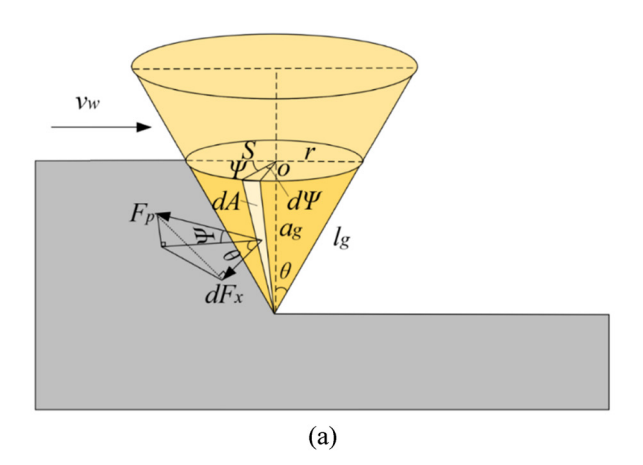
$$F_{t,pg} = N_{d,pl}F'_{t,pg} = \frac{\pi}{4}N_{d,pl}C_3\left(\frac{v_w}{v_s}\right)^{\alpha}a_p^{\beta}d_s^{\gamma} \sin \theta$$

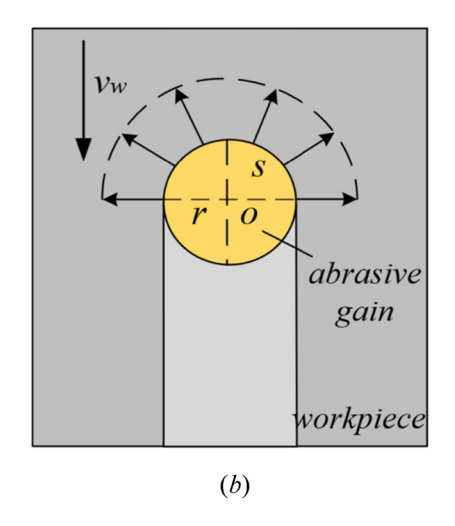
$$= k_4b\left(\frac{v_w}{v_s}\right)^{\alpha}a_p^{\beta}d_s^{\gamma} \sin \theta$$

$$= K_{d,pl}F'_{n,pg} = N_{d,pl}C_3\left(\frac{v_w}{v_s}\right)^{\alpha}a_p^{\beta}d_s^{\gamma} \sin \theta \tan \theta$$

$$= k_5b\left(\frac{v_w}{v_s}\right)^{\alpha}a_p^{\beta}d_s^{\gamma} \sin \theta \tan \theta,$$
(19)

where, α , β , γ are the constants, respectively, $k_4 = \frac{\pi C_3}{4} \xi_{\rm pl}$, and $k_5 = C_3 \xi_{\rm pl}$.





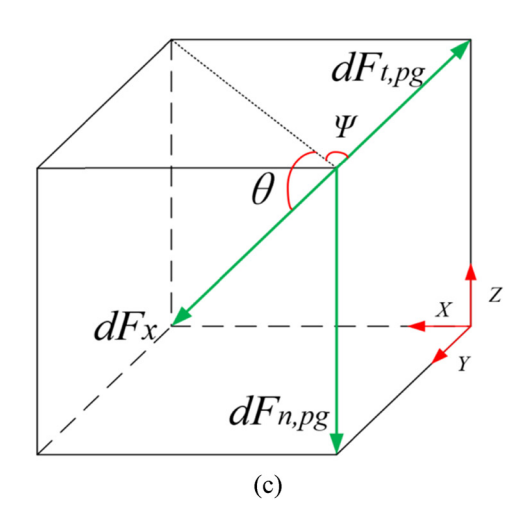


Figure 2: Diagram of plowing force. (a) The relationship between the grinding force per unit area and its component force dF_x in any direction is plotted, (b) detailed map of S-region plowing force, and (c) simplified diagram of tangential plowing force and normal plowing force.

At the same time, the friction coefficient between the workpiece-grinding wheel contact surface in the plowing stage can be obtained as follows:

$$\mu_{\rm pl} = \frac{F_{\rm t,pl}}{F_{\rm n,pl}} = \frac{\pi}{4 \tan \theta}.$$
(20)

2.3 Chip formation force

At this stage, the workpiece material is sheared by the cutting edge of the tool to form chips. Therefore, the grinding force prediction model at this stage can be established by the characteristics of the material.

Typically, the energy consumed to remove the unit volume of material is recorded as the grinding specific energy [38], which is expressed by u:

$$u = \frac{v_{\rm s} F_{\rm t}}{b v_{\rm w} a_{\rm p}}.$$
 (21)

Therefore, the grinding specific energy u_{ch} of a single abrasive grain in the chip formation stage can be regarded as

$$u_{\rm ch} = \frac{v_{\rm s} F_{\rm t, ch}}{b v_{\rm w} a_{\rm p}}.$$
 (22)

In general, the grinding specific energy $u_{\rm ch}$ can be divided into two parts: static grinding specific energy $u_{\rm ch,st}$ and dynamic grinding specific energy $u_{\rm ch,dy}$ [47].

$$u_{\rm ch} = u_{\rm ch,st} + u_{\rm ch,dy}. \tag{23}$$

The specific energy of static grinding is a constant, which is determined by the material properties of work-piece-grinding wheel. The dynamic specific grinding energy is determined by the workpiece and grinding wheel materials and grinding parameters.

2.3.1 Shear strain effect of material removal process

In the case of shear deformation, the general form of the dynamic-plasticity constitutive relation of the material is [49]

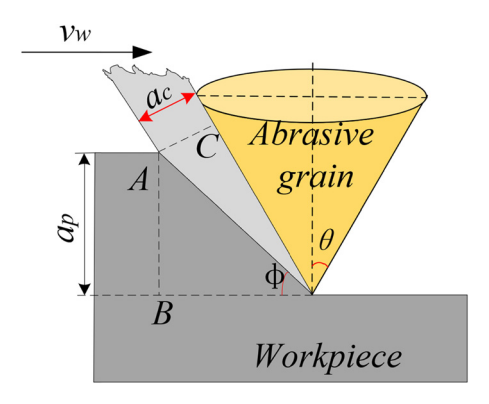


Figure 3: Single grain negative rake angle shear deformation diagram.

$$\tau = h(\gamma, \gamma', T), \tag{24}$$

where τ is the shear flow stress, γ is the shear strain, γ' is the shear strain rate, and T is the deformation temperature.

Figure 3 shows the negative rake angle shear deformation diagram of single grain grinding. In general, with the increase in the shear strain γ and the shear strain rate γ' , the shear flow stress τ of the material also increases. With the increase in the deformation temperature T, the shear flow stress τ of the material will decrease. The dynamic specific grinding energy $u_{\rm ch,dy}$ is proportional to the change in the shear flow stress τ , which is the result of multiple effects.

2.3.2 Shear strain effect

The negative rake angle shear deformation diagram of a single abrasive grain acting on the workpiece is shown in Figure 3. Under two-dimensional shear conditions, γ and γ' in the shear band can be expressed as follows:

$$\gamma = \frac{\cos \theta}{\sin \phi \cos(\phi + \theta)},\tag{25}$$

$$\gamma' = \frac{v_{\rm s} \cos \theta}{\Delta s \cos(\phi + \theta)},\tag{26}$$

where ϕ is the shear angle, and Δs is the thickness of shear band.

The relationship between the shear band thickness Δs and the average undeformed chip thickness a_c is [49]

$$\frac{a_{\rm c}}{\Delta s \sin \phi} \approx 10. \tag{27}$$

The relationship between the average undeformed chip thickness $a_{\rm c}$ of a single abrasive grain and the grinding depth $a_{\rm p}$ is

$$\kappa = \frac{a_{\rm c}}{a_{\rm p}} = \frac{\sin \phi}{\cos(\phi + \theta)}.$$
 (28)

Therefore,

$$\gamma' = \frac{v_{\rm s} \cos \theta}{\Delta s \cos(\phi + \theta)} = \frac{10v_{\rm s} \cos \theta}{a_{\rm c} \cos(\phi + \theta)}.$$
 (29)

Therefore, the shear strain rate γ' is proportional to the wheel speed ν_s and inversely proportional to the average undeformed chip thickness a_c .

It is noted that ϕ and a_c are physical quantities related to the grinding parameters, and based on empirical equations

$$\gamma' = k_6 d_s^e v_s^f a_p^g v_w^{1-f}, (30)$$

where k_6 is a constant.

2.4 Calculation of force in chip formation stage

Studies have shown that there is the following relationship between dynamic special grinding specific energy $u_{ch,dy}$ and shear strain rate y' [38].

$$u_{\text{ch,dy}} = k_7 \ln \left(\frac{\gamma'}{\gamma'_0} \right) = k_7 \ln \left(\frac{10v_s \cos \theta}{\gamma'_0 a_c \cos(\phi + \theta)} \right)$$
$$= k_7 \ln \left(\frac{k_6 d_s^e v_s^f a_p^g v_w^{1-f}}{\gamma'_0} \right). \tag{31}$$

where k_7 and y_0' are constants.

Thus,

$$u_{\rm ch} = \lambda u_{\rm ch,dy} = \lambda k_7 \ln \left(\frac{k_6 d_{\rm s}^{0.25} v_{\rm s}^{1.5} a_{\rm p}^{-0.25} v_{\rm w}^{-0.5}}{\gamma_0'} \right)$$

$$= k_8 \ln \left(\frac{k_6 d_{\rm s}^{\rm e} v_{\rm s}^{\rm f} a_{\rm p}^{\rm g} v_{\rm w}^{1-\rm f}}{\gamma_0'} \right). \tag{32}$$

According to Eqs. (24) and (32) can be obtained.

$$F'_{t,ch} = \frac{u_{ch}bv_{w}a_{p}}{v_{s}} = k_{8} \ln \left(\frac{k_{6}d_{s}^{e}v_{s}^{f}a_{p}^{g}v_{w}^{1-f}}{\gamma'_{o}} \right) \frac{bv_{w}a_{p}}{v_{s}}.$$
 (33)

where $k_8 = \lambda k_7$.

Therefore.

$$F_{t,ch} = F'_{t,ch} \cdot N_{d,ch} = k_8 \ln \left(\frac{k_6 d_s^e v_s^f a_p^g v_w^{1-f}}{\gamma'_0} \right) \frac{b v_w a_p^{1.5} d_s^{0.5}}{v_s}. (34)$$

It was shown that the coefficient of friction between the abrasive grains-workpiece during the grinding stage is

$$\mu_{\rm ch} = \frac{\pi}{4 \tan 60^{\circ}}.$$
 (35)

Therefore,

$$F_{n,ch} = \frac{F_{t,ch}}{\mu_{ch}} = k_8 \ln \left(\frac{k_6 d_s^e v_s^f a_p^g v_w^{1-f}}{\gamma_0'} \right) \frac{b v_w a_p^{1.5} d_s^{0.5}}{v_s}$$

$$\cdot \frac{4 \tan 60^\circ}{\pi}$$

$$= k_9 \ln \left(\frac{k_6 d_s^e v_s^f a_p^g v_w^{1-f}}{\gamma_0'} \right) \frac{b v_w a_p^{1.5} d_s^{0.5}}{v_s},$$
(36)

where, $k_9 = k_8 \frac{4 \tan 60^{\circ}}{\pi}$.

2.5 Summary

This can be obtained from Eqs. (10), (12), (19), (34), and (36).

$$\begin{cases} F_{n} = F_{n,sl} + F_{t,pg} + F_{t,ch} = k_{l} \frac{a_{p}^{0.5} v_{w} b}{v_{s} d_{s}^{0.5}} \\ + k_{s} b \left(\frac{v_{w}}{v_{s}}\right)^{a} a_{p}^{\beta} d_{s}^{\gamma} \sin \theta \tan \theta \\ + k_{9} \ln \left(\frac{k_{6} d_{s}^{e} v_{s}^{f} a_{p}^{g} v_{w}^{1-f}}{y_{0}^{\prime}}\right) \frac{b v_{w} a_{p}^{1.5} d_{s}^{0.5}}{v_{s}} \end{cases}$$

$$\begin{cases} F_{t} = F_{t,sl} + F_{t,pg} + F_{t,ch} = k_{3} \frac{a_{p}^{0.5} v_{w} b}{v_{s} d_{s}^{0.5}} \\ \times \left(\frac{C_{1} \overline{S}}{F_{n,sl}} + C_{2}\right) \frac{v_{s} + 2\pi f A}{\sqrt{(2\pi f A)^{2} + v_{s}^{2}}} \\ + k_{4} b \left(\frac{v_{w}}{v_{s}}\right)^{a} a_{p}^{\beta} d_{s}^{\gamma} \sin \theta \\ + k_{8} \ln \left(\frac{k_{6} d_{s}^{e} v_{s}^{f} a_{p}^{g} v_{w}^{1-f}}{y_{0}^{\prime}}\right) \frac{b v_{w} a_{p}^{1.5} d_{s}^{0.5}}{v_{s}}. \end{cases}$$

3 Experimental verification platform

Through the above theoretical analysis, the predictive force model of UAG of γ -TiAl intermetallic compounds has been established. In order to solve the unknowns in Eq. (37) and verify the predictive force model, a corresponding experimental verification platform is needed. This section introduces the experimental verification platform.

The VMC-850 vertical machining center is selected to build a platform for the main body of the grinding test. A one-dimensional longitudinal vibration ultrasonic system is installed on the spindle to realize the longitudinal ultrasonic vibration of the grinding wheel. At the same time,

Kistler 9257 B dynamometer, 5070 multi-channel charge amplifier, 5697 data acquisition card, and DynoWare software are used to collect normal grinding force F_n and tangential grinding force F_t . One-dimensional longitudinal vibration ultrasonic grinding test platform is shown in Figure 4.

The test used an ordered diamond grinding wheel with an average particle size of 115 μ m. The width and diameter of the grinding wheel are 10 mm and 20 mm, respectively. The workpiece is γ -TiAl intermetallic compounds (Ti-45Al-2Mn-2Nb), Table 1 shows the material parameters of γ -TiAl [3]. The length of the workpiece along the grinding direction is 30 mm, and the radial width along the grinding wheel is 15 mm. The workpiece is clamped on the worktable by a fixture. The ultrasonic frequency is 35 kHz.

4 Model calculation and verification

4.1 Calculation of unknown coefficients of the model

Since Eq. (37) contains some unknown vectors, the model is not complete and cannot predict the grinding force of UAG of γ -TiAl intermetallic compounds. Therefore, it is necessary to obtain the grinding force value through experiments to solve the unknown coefficients.

12 groups of experimental results are randomly selected, as shown in Table 2, and the data in the table are substituted in formula (37) to solve the unknown coefficient. The results are shown in Table 3.

Substitute the unknown coefficient in Eq. (37).

$$\begin{cases} F_{\rm n} = F_{\rm n,sl} + F_{\rm t,pg} + F_{\rm t,ch} = 10.75 \frac{a_{\rm p}^{0.5} v_{\rm w} b}{v_{\rm s} d_{\rm s}^{0.5}} \\ + 0.74 \left(\frac{v_{\rm w}}{v_{\rm s}}\right)^{0.047} a_{\rm p}^{0.33} d_{\rm s}^{1.56} b \sin \theta \tan \theta \\ + 1.01 \ln(4.29 d_{\rm s}^{0.64} v_{\rm s}^{-0.22} a_{\rm p}^{-0.48} v_{\rm w}^{1.22}) \frac{v_{\rm w} a_{\rm p}^{1.5} d_{\rm s}^{0.5} b}{v_{\rm s}} \\ F_{\rm t} = F_{\rm t,sl} + F_{\rm t,pg} + F_{\rm t,ch} = -2.18 \frac{a_{\rm p}^{0.5} v_{\rm w} b}{v_{\rm s} d_{\rm s}^{0.5}} \\ \times \left(\frac{288.17}{F_{\rm n,sl}} - 25.27\right) \frac{v_{\rm s} + 2\pi f A}{\sqrt{(2\pi f A)^2 + v_{\rm s}^2}} \\ + 0.22 \left(\frac{v_{\rm w}}{v_{\rm s}}\right)^{0.047} a_{\rm p}^{0.33} d_{\rm s}^{1.56} b \sin \theta \\ + 11.23 \ln(4.29 d_{\rm s}^{0.64} v_{\rm s}^{-0.22} a_{\rm p}^{-0.48} v_{\rm w}^{1.22}) \frac{v_{\rm w} a_{\rm p}^{1.5} d_{\rm s}^{0.5} b}{v_{\rm s}}. \end{cases}$$

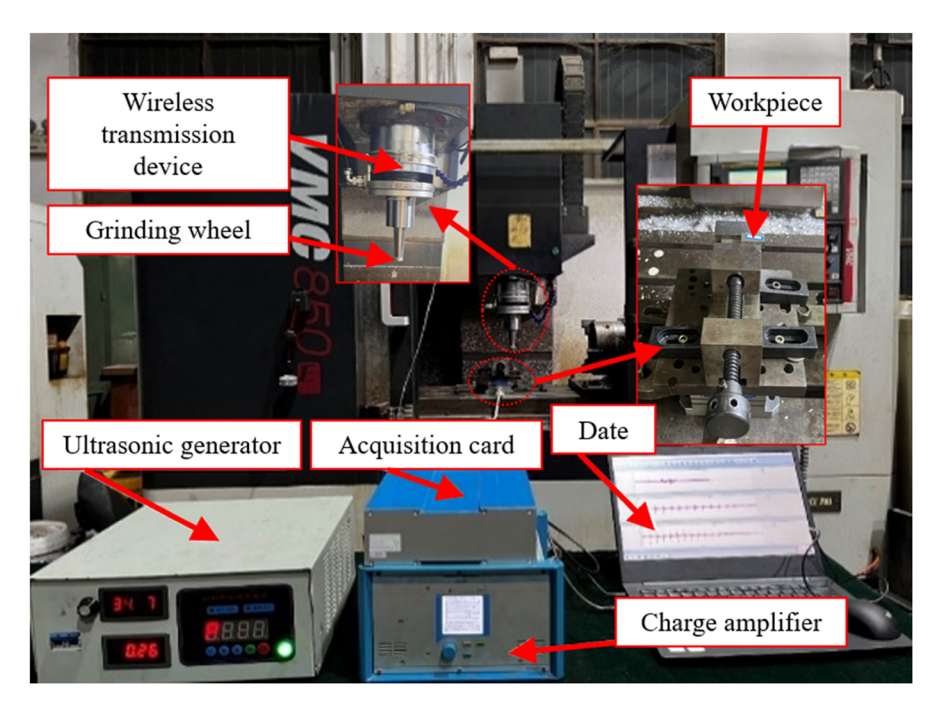


Figure 4: One-dimensional longitudinal vibration ultrasonic grinding test platform.

Table 1: Mechanical properties of y-TiAl intermetallic compounds

Density	Elastic	Yield	Ductility at room	Creep	Antioxidation limit (°C)	
(g·cm ^{−3})	modulus (GPa)	strength (MPa)	temperature (%)	limit (°C)		
3.7-3.9	160–176	450-630	1–4	1,000	900-1,000	

Table 2: Twelve groups of experimental results for calculating unknown coefficients

a _p (mm)	v _w (mm×min ⁻¹)	v _s (rpm)	A (mm)	F _n	$F_{t}(N)$
0.002	150	3,000	0.002	8.41	4.15
0.002	200	4,000	0.004	6.68	3.53
0.002	250	5,000	0.006	3.22	3.08
0.004	150	2,000	0.004	13.79	7.36
0.004	100	3,000	0.006	8.39	4.72
0.004	250	4,000	0	15.41	7.93
0.004	200	5,000	0.002	15.98	6.79
0.006	200	2,000	0.006	7.02	4.72
0.006	250	3,000	0.004	16.99	8.66
0.008	200	3,000	0	17.88	9.16
0.008	150	4,000	0.006	10.5	4.75
0.008	100	5,000	0.004	9.14	3.37

4.2 Model validation

By solving the unknown quantities in the model, the complete prediction formula of the grinding force of UAG γ -TiAl intermetallic compounds was obtained. However, the accuracy of the prediction model still has some unknowns. Therefore, it is necessary to compare the predicted value of grinding force with the experimental value under different processing parameters to verify the rationality of the model.

Figure 5 shows the comparison between the predicted value and the actual value of the model at different grinding depths $a_{\rm p}$ under $\nu_{\rm w}$ = 150 mm · min⁻¹, $\nu_{\rm s}$ = 4,000 rpm, A = 4 µm. It can be seen from Figure 5 that the maximum deviation between the predicted value and the actual value of $F_{\rm t}$ under different grinding depth conditions is 20%, and the maximum deviation between the predicted value and the actual value of $F_{\rm n}$ is 19%. And with the increase in $a_{\rm p}$, the grinding force also showed an upward trend, which is in line with the basic law.

Figure 6 shows the comparison between the predicted value and the actual value of the model at $a_{\rm p}$ = 4 μ m, $v_{\rm s}$ = 4,000 rpm, A = 4 μ m, for different feed rates $v_{\rm w}$. It can be seen from Figure 6 that the maximum deviation of the predicted value of $F_{\rm t}$ from the actual value is 23%

Table 3: UAG of y-TiAl intermetallic compounds unknown coefficient values

k_1	k ₃	k_4	k ₅	$\frac{k_6}{v_0'}$	k ₈	k 9	α	β	γ
10.75 $C_1\bar{S}$ 288.17	−2.18 C ₂ −25.27	0.22 e 0.64	0.74 f -0.22	4.29 g -0.48	11.23	1.01	0.047	0.33	1.56

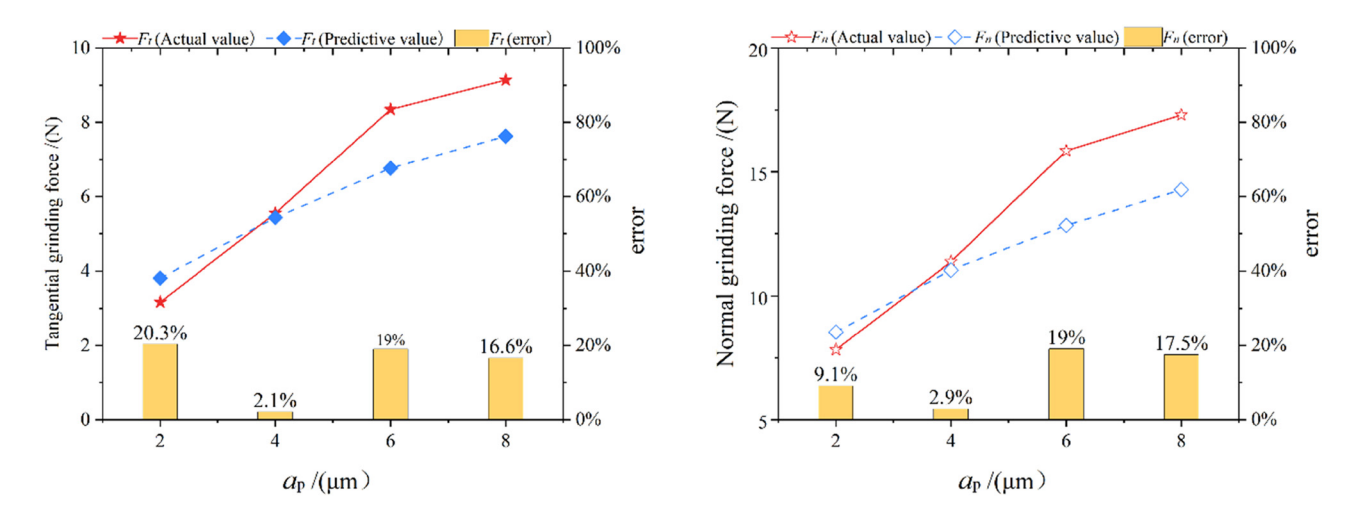


Figure 5: Comparison between the predicted value and the actual value of the model at different grinding depths a_p : $v_w = 150 \text{ mm} \cdot \text{min}^{-1}$, $v_s = 4,000 \text{ rpm}$, $A = 4 \mu \text{m}$.

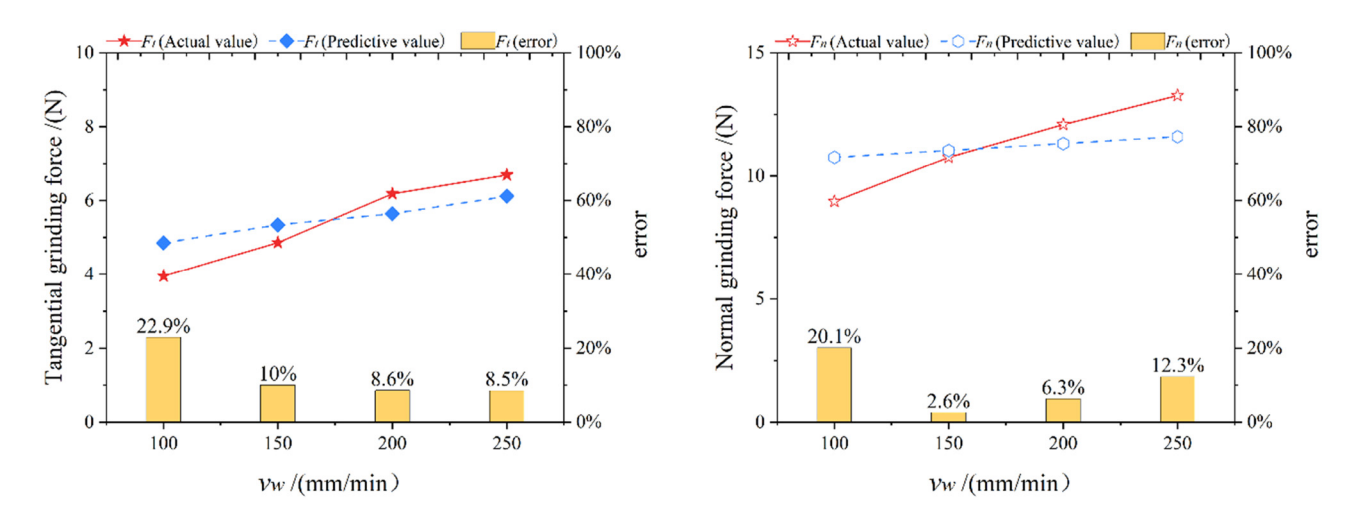


Figure 6: Comparison between the predicted value and the actual value of the model at different feed speeds v_w : $a_p = 4 \mu m$, $v_s = 4,000 \text{ rpm}$, $A = 4 \mu m$.

and the maximum deviation of the predicted value of F_n from the actual value is 20.1% at different feed rates. And as ν_w increases, the grinding force tends to increase, which is in accordance with the law.

Figure 7 shows the comparison between the predicted value and the actual value of the model at $a_p = 4 \mu m$,

 $v_{\rm w}$ = 150 mm · min⁻¹, A = 4 µm and different grinding wheel speeds $v_{\rm s}$. It can be seen from Figure 7 that at different speeds, the maximum deviation between the predicted value and the actual value of $F_{\rm t}$ is 16%, and the maximum deviation between the predicted value and the actual value of $F_{\rm n}$ is 20.3%. Moreover, with the increase in

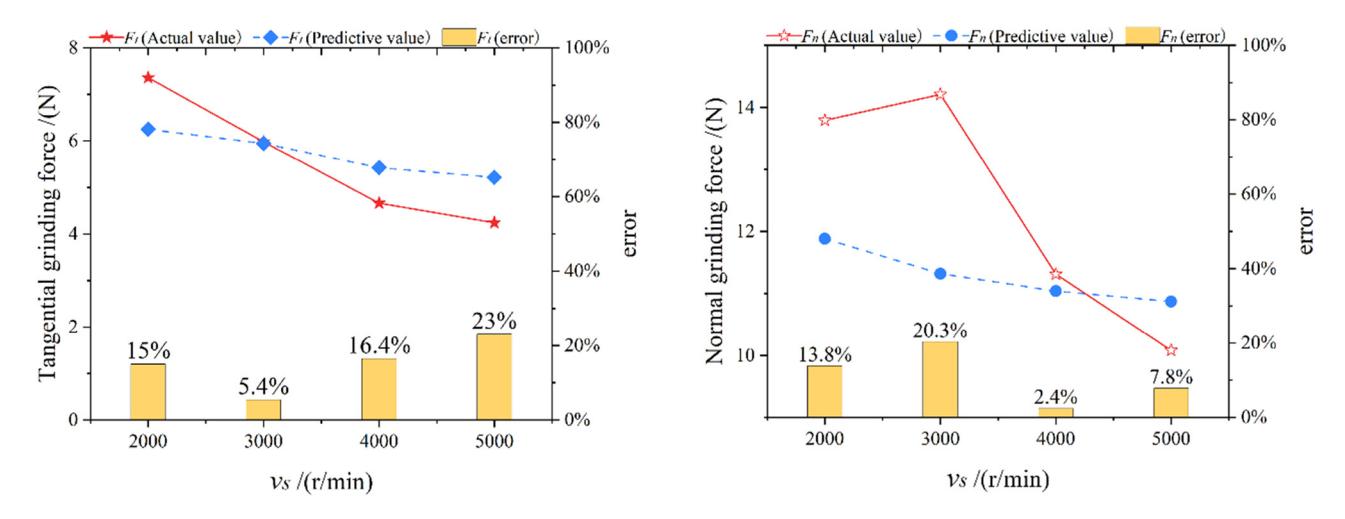


Figure 7: Comparison between the predicted value and the actual value of the model at different grinding wheel speeds v_s : $a_p = 4 \mu m$, $v_w = 150 \text{ mm} \cdot \text{min}^{-1}$, $A = 4 \mu m$.

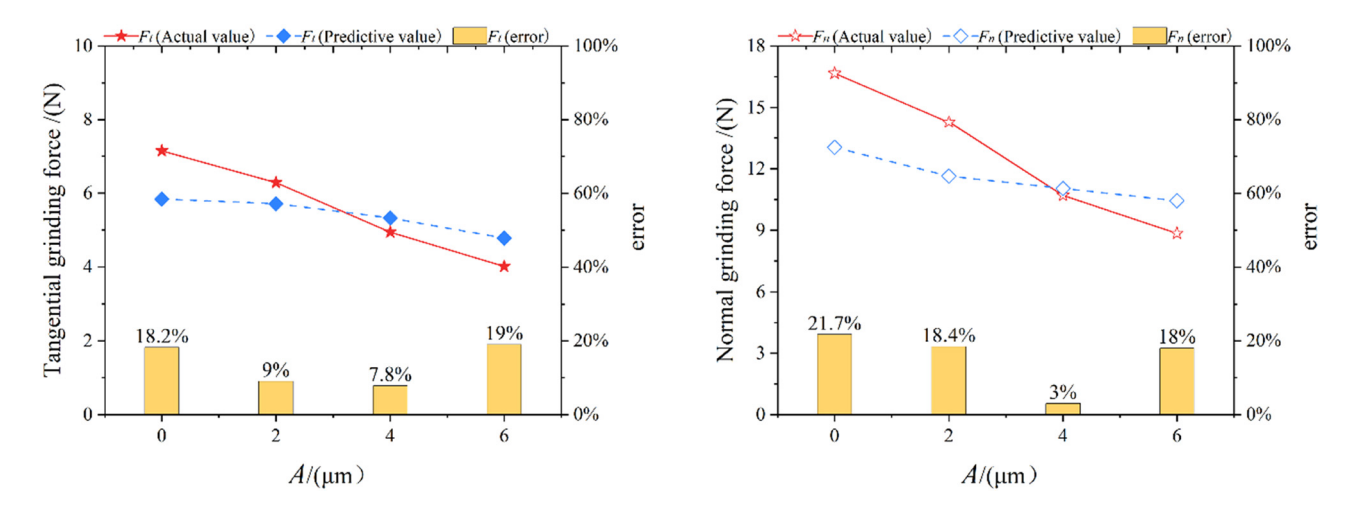


Figure 8: Comparison between the predicted value and the actual value of the model at different ultrasonic amplitudes $A: a_p = 4 \mu m$, $v_w = 150 \text{ mm} \cdot \text{min}^{-1}$, $v_s = 4,000 \text{ rpm}$.

 v_s , the grinding force also shows a decreasing trend, which is in accordance with the law.

Figure 8 shows the comparison between the predicted value and the actual value of the model at different ultrasonic amplitudes of A, $a_{\rm p}=4~\mu{\rm m}$, $v_{\rm w}=150~{\rm mm\cdot min^{-1}}$, $v_{\rm s}=4,000~{\rm rpm}$. It can be seen from Figure 8 that under different ultrasonic amplitudes, the maximum deviation between the predicted value of $F_{\rm t}$ and the actual value is 23%, and the maximum deviation between the predicted value and the actual value of $F_{\rm n}$ is 21.7%. With the increase in A, the grinding force also shows an upward trend, which conforms to the law.

Therefore, the maximum deviation between the predicted value and the actual value of F_t is 23%, and the maximum deviation between the predicted value and the

actual value of $F_{\rm n}$ is 21.7%. The results show that the predicted results are in good agreement with the experimental results.

5 Conclusion

In this study, a new UAG force prediction model is established. The model considers three key factors: the friction between the abrasive and the material, the plastic deformation of the material during the abrasive plowing process, and the shear strain effect of the material during the chip formation process. Based on this model, the UAG experiment of γ -TiAl intermetallic compounds was carried

out, and the unknown coefficients in the model were calculated.

The model was verified under different parameters. It was found that the maximum deviation between the predicted value and the actual value of $F_{\rm t}$ is 23%, and the maximum deviation between the predicted value and the actual value of $F_{\rm n}$ is 21.7%. The results show that the predicted results are in good agreement with the experimental results.

In addition, by modifying the correlation coefficient, the model can be used to predict the grinding force of different metal materials under different processing parameters.

Acknowledgments: The authors are thankful for the financial support from the National Natural Science Funds of China (U1904170), the China Postdoctoral Science Foundation (2022M711054), and Henan Natural Science Youth Progra (232300420302).

Funding information: This study was supported by the financial supports from the National Natural Science Funds of China (U1904170), the China Postdoctoral Science Foundation (2022M711054), and Henan Natural Science Youth Program (232300420302).

Author contributions: Zhenhao Li and Zhibo Yang organized and conceived the project, and analyzed and arranged data; Song Yang, Xiaoning Liu, and Guoqing Xiao conducted the experiments; Hongzhan San, Yanru Zhang, and Wei Wang helped perform the analysis with constructive discussions. All authors have accepted responsibility for the entire content of this manuscript and approved its submission.

Conflict of interest: The authors state no conflict of interest

Data availability statement: The datasets generated and/ or analyzed during the current study are available from the corresponding author on reasonable request.

References

- [1] Babu, R. P., K. V. Vamsi, and S. Karthikeyan. On the formation and stability of precipitate phases in a near lamellar y-TiAl based alloy during creep. *Intermetallics*, Vol. 98, 2018, pp. 115–125.
- [2] Cui, X. P., H. Ding, Y. Y. Zhang, Y. Yao, G. H. Fan, L. J. Huang, et al. Fabrication, microstructure characterization and fracture behavior of a unique micro-laminated TiB-TiAl composites. *Journal of Alloys and Compounds*, Vol. 775, 2018, pp. 1057–1067.
- [3] Xia, Z. W., C. W. Shan, M. H. Zhang, M. C. Cui, and M. Luo. Machinability of γ-TiAl: A review. *Chinese Journal of Aeronautics*, Vol. 36, No. 7, 2023, pp. 40–75.

- [4] Qi, H., S. K. Qin, Z. C. Cheng, Q. Teng, T. Hong, and Y. Xie. Towards understanding performance enhancing mechanism of micro-holes on K9 glasses using ultrasonic vibration-assisted abrasive slurry jet. *Journal of Manufacturing Processes*, Vol. 64, 2021, pp. 585–593.
- [5] Li, H. N., Y. J. Zhao, S. Y. Cao, H. Chen, C. Q. Wu, H. Qi, et al. Controllable generation of 3D textured abrasive tools via multiplepass laser ablation. *Journal of Materials Processing Technology*, Vol. 295, 2021, id. 117149.
- [6] Cao, Y., Y. J. Zhu, W. F. Ding, Y. T. Qiu, L. F. Wang, and J. H. Xu. Vibration coupling effects and machining behavior of ultrasonic vibration plate device for creep-feed grinding of Inconel 718 nickel-based superalloy. *Chinese Journal of Aeronautics*, Vol. 35, No. 2, 2022, pp. 332–345.
- [7] Cao, Y., Y. J. Zhu, H. N. Li, L. F. Wang, H. H. Su, Z. Yin, et al. Development and performance of a novel ultrasonic vibration plate sonotrode for grinding. *Journal of Manufacturing Processes*, Vol. 57, 2020, pp. 174–186.
- [8] Yang, Y. Y., M. Yang, C. H. Li, R. Z. Li, Z. Said, H. M. Ali, et al. Machinability of ultrasonic vibration-assisted micro-grinding in biological bone using nanolubricant. Frontiers of Mechanical Engineering, Vol. 18, No. 1, 2023, id. 1.
- [9] Jin, J. W., X. B. Wang, W. B. Bie, F. Chen, and B. Zhao. Machinability of SiC_r/SiC ceramic matrix composites using longitudinal-torsional coupled rotary ultrasonic machining. *The International Journal of Advanced Manufacturing Technology*, Vol. 2023, 2023, pp. 1–2.
- [10] Chen, F., W. B. Bie, X. B. Wang, and B. Zhao. Longitudinal-torsional coupled rotary ultrasonic machining of ZrO₂ ceramics: An experimental study. *Ceramics International*, Vol. 48, No. 19, 2022, pp. 28154–28162.
- [11] Huang, B., W. H. Wang, Y. F. Xiong, X. F. Wu, J. T. Liu, C. Liu, et al. Investigation of force modeling in ultrasonic vibration-assisted drilling SiC_f/SiC ceramic matrix composites. *Journal of Manufacturing Processes*, Vol. 96, 2023, pp. 21–30.
- [12] Chen, Y. R., H. H. Su, N. Qian, J. Y. He, J. Q. Gu, J. H. Xu, et al. Ultrasonic vibration-assisted grinding of silicon carbide ceramics based on actual amplitude measurement: Grinding force and surface quality. *Ceramics International*, Vol. 47, No. 11, 2021, pp. 15433–15441.
- [13] Zai, P. H., J. L. Tong, Z. Q. Liu, Z. P. Zhang, C. S. Song, and B. Zhao. Analytical model of exit burr height and experimental investigation on ultrasonic-assisted high-speed drilling micro-holes. *Journal of Manufacturing Processes*, Vol. 68, 2021, pp. 807–817.
- [14] Han, G. H., W. Q. Wan, Z. C. Zhang, L. H. Xu, F. C. Liu, and H. O. Zhang. Experimental investigation into effects of different ultrasonic vibration modes in micro-extrusion process. *Journal of Manufacturing Processes*, Vol. 67, 2021, pp. 427–437.
- [15] Wang, Y., V. K. Sarin, B. Lin, H. Li, and S. Gillard. Feasibility study of the ultrasonic vibration filing of carbon fiber reinforced silicon carbide composites. *International Journal of Machine Tools and Manufacture*, Vol. 101, 2016, pp. 10–17.
- [16] Dong, G. J., C. Y. Lang, C. Li, and L. M. Zhang. Formation mechanism and modelling of exit edge-chipping during ultrasonic vibration grinding of deep-small holes of microcrystalline-mica ceramics. *Ceramics International*, Vol. 46, No. 8, 2020, pp. 12458–12469.
- [17] Yuan, Z. J., D. H. Xiang, P. C. Peng, Z. Q. Zhang, B. H. Li, M. Y. Ma, et al. A comprehensive review of advances in ultrasonic vibration machining on SiCp/Al composites. *Journal of Materials Research and Technology*, Vol. 24, 2023, pp. 6665–6698.

- [18] Miao, Q., W. F. Ding, J. H. Xu, L. J. Cao, H. C. Wang, Z. Yin, et al. Creep feed grinding induced gradient microstructures in the superficial layer of turbine blade root of single crystal nickel-based superalloy. *International Journal of Extreme Manufacturing*, Vol. 3, No. 4, 2021, id. 045102.
- [19] Cao, Y., J. F. Yin, W. F. Ding, and J. H. Xu. Alumina abrasive wheel wear in ultrasonic vibration-assisted creep-feed grinding of Inconel 718 nickel-based superalloy. *Journal of Materials Processing Technology*, Vol. 297, 2021, id. 117241.
- [20] Chen, C. S., J. Y. Tang, H. F. Chen, and B. Zhao. An active manufacturing method of surface micro structure based on ordered grinding wheel and ultrasonic-assisted grinding. *The International Journal of Advanced Manufacturing Technology*, Vol. 97, No. 5–8, 2018, pp. 1627–1635.
- [21] Yang, Z. B., D. Y. He, W. Sun, Y. Q. Zhang, S. Y. Zhang, H. B. Shi, et al. Determination of the grinding force on optical glass based on a diamond wheel with an ordered arrangement of abrasive grains. *The International Journal of Advanced Manufacturing Technology*, Vol. 115, No. 4, 2021, pp. 1237–1248.
- [22] Zhong, B. F., J. Q. Dang, Q. L. An, and M. Chen. Surface morphologies and microstructure of high-strength steel AISI 4820 with different heat treatment during grinding process. *Journal of Manufacturing Processes*, Vol. 96, 2023, pp. 1–10.
- [23] Yang, H., J. Xie, Q. P. He, J. H. Liu, and Y. Q. Shi. Study on diamond cutting-to-burnishing for thermal-force dispersion in dry metal grinding. *Journal of Materials Processing Technology*, Vol. 313, 2023, id. 117874.
- [24] Cui, X., C. H. Li, W. F. Ding, Y. Chen, C. Miao, X. F. Xu, et al. Minimum quantity lubrication machining of aeronautical materials using carbon group nanolubricant: From mechanisms to application. *Chinese Journal of Aeronautics*, Vol. 35, No. 11, 2022, pp. 85–112.
- [25] Ding, W. F., C. W. Dai, T. Y. Yu, J. H. Xu, and Y. C. Fu. Grinding performance of textured monolayer CBN wheels: Undeformed chip thickness nonuniformity modeling and ground surface topography prediction. *International Journal of Machine Tools and Manufacture*, Vol. 122, 2017, pp. 66–80.
- [26] Xi, X. X., W. F. Ding, Y. C. Fu, and J. H. Xu. Grindability evaluation and tool wear during grinding of Ti₂AlNb intermetallics. *The International Journal of Advanced Manufacturing Technology*, Vol. 94, No. 1–4, 2018, pp. 1441–1450.
- [27] Xi, X. X., W. F. Ding, Z. X. Wu, and L. Anggei. Performance evaluation of creep feed grinding of γ-TiAl intermetallics with electroplated diamond wheels. *Chinese Journal of Aeronautics*, Vol. 34, No. 6, 2021, pp. 100–109.
- [28] Hood, R., F. Lechner, D. K. Aspinwall, and W. Voice. Creep feed grinding of gamma titanium aluminide and burn resistant titanium alloys using SiC abrasive. *International Journal of Machine Tools and Manufacture*, Vol. 47, No. 9, 2007, pp. 1486–1492.
- [29] Bhaduri, D., S. L. Soo, D. K. Aspinwall, D. Novovic, S. Bohr, P. Harden, et al. Ultrasonic assisted creep feed grinding of gamma titanium aluminide using conventional and superabrasive wheels. CIRP Annals – Manufacturing Technology, Vol. 66, No. 1, 2017, pp. 341–344.
- [30] Chen, T., Y. J. Zhu, X. X. Xi, H. X. Huan, and W. F. Ding. Process parameter optimization and surface integrity evolution in the highspeed grinding of TiAl intermetallics based on grey relational analysis method. *The International Journal of Advanced Manufacturing Technology*, Vol. 117, No. 9–10, 2021, pp. 2895–2908.

- [31] Li, B. K., C. H. Li, Y. B. Zhang, Y. G. Wang, D. Z. Jia, Z. Yang, et al. Heat transfer performance of MQL grinding with different nanofluids for Ni-based alloys using vegetable oil. *Journal of Cleaner Production*, Vol. 154, 2017, pp. 1–11.
- [32] Guo, Q., W. B. Wang, Y. Jiang, and Y. W. Sun. 3D surface topography prediction in the five-axis milling of plexiglas and metal using cutters with non-uniform helix and pitch angles combining runout. *Journal of Materials Processing Technology*, Vol. 314, 2023, id. 117885.
- [33] Hou, Z. B. and R. Komanduri. On the mechanics of the grinding process – Part I. Stochastic nature of the grinding process. *International Journal of Machine Tools and Manufacture*, Vol. 43, No. 15, 2003, pp. 1579–1593.
- [34] Durgumahanti, U. S. P., V. Singh, and P. V. Rao. A new model for grinding force prediction and analysis. *International Journal of Machine Tools and Manufacture*, Vol. 50, No. 3, 2010, pp. 231–240.
- [35] Jiang, J. L., P. Q. Ge, S. F. Sun, D. X. Wang, Y. L. Wang, and Y. Yang. From the microscopic interaction mechanism to the grinding temperature field: An integrated modelling on the grinding process. *International Journal of Machine Tools and Manufacture*, Vol. 110, 2016, pp. 27–42.
- [36] Li, H. N., T. B. Yu, Z. X. Wang, L. D. Zhu, and W. S. Wang. Detailed modeling of cutting forces in grinding process considering variable stages of grain-workpiece micro interactions. *International Journal* of Mechanical Sciences, Vol. 126, 2017, pp. 319–339.
- [37] Zhang, Y. B., C. H. Li, H. J. Ji, X. H. Yang, M. Yang, D. Z. Jia, et al. Analysis of grinding mechanics and improved predictive force model based on material-removal and plastic-stacking mechanisms. *International Journal of Machine Tools and Manufacture*, Vol. 122, 2017, pp. 81–97.
- [38] Li, B. K., C. W. Dai, W. F. Ding, C. Y. Yang, C. H. Li, O. Kulik, et al. Prediction on grinding force during grinding powder metallurgy nickel-based superalloy FGH96 with electroplated CBN abrasive wheel. *Chinese Journal of Aeronautics*, Vol. 34, No. 8, 2021, pp. 65–74.
- [39] Ma, X. F., Z. Q. Cai, B. Yao, G. F. Chen, W. S. Liu, and K. X. Qiu. Dynamic grinding force model for face gear based on the wheelgear contact geometry. *Journal of Materials Processing Technology*, Vol. 306, 2022, id. 117633.
- [40] Yi, J., T. Yi, H. Deng, B. Chen, and W. Zhou. Theoretical modeling and experimental study on grinding force of straight groove structured grinding wheel. *The International Journal of Advanced Manufacturing Technology*, Vol. 124, No. 10, 2023, pp. 3407–3421.
- [41] Duan, Z. J., C. H. Li, Y. B. Zhang, M. Yang, T. Gao, X. Liu, et al. Mechanical behavior and semiempirical force model of aerospace aluminum alloy milling using nano biological lubricant. Frontiers of Mechanical Engineering, Vol. 18, No. 3, 2023, id. 4.
- [42] Liu, M. Z., C. H. Li, Y. B. Zhang, M. Yang, T. Gao, X. Cui, et al. Analysis of grinding mechanics and improved grinding force model based on randomized grain geometric characteristics. *Chinese Journal of Aeronautics*, Vol. 36, No. 7, 2023, pp. 160–193.
- [43] Liu, M. Z., C. H. Li, Y. B. Zhang, M. Yang, T. Gao, X. Cui, et al. Analysis of grain tribology and improved grinding temperature model based on discrete heat source. *Tribology International*, Vol. 180, 2023, id. 108196.
- [44] Abdelkawy, A., M. Hossam, and H. El-Hofy. Mathematical model of thrust force for rotary ultrasonic drilling of brittle materials based on the ductile-to-brittle transition phenomenon. *The International*

- *Journal of Advanced Manufacturing Technology*, Vol. 101, No. 1–4, 2019, pp. 801–813.
- [45] Lei, X. F., D. H. Xiang, P. C. Peng, G. F. Liu, B. Li, B. Zhao, et al. Establishment of dynamic grinding force model for ultrasonicassisted single abrasive high-speed grinding. *Journal of Materials Processing Technology*, Vol. 300, 2022, id. 117420.
- [46] Zhang, M. H., Z. W. Xia, C. W. Shan, and M. Luo. Analytical model of grinding force for ultrasonic-assisted grinding of C_f/SiC composites. *The International Journal of Advanced Manufacturing Technology*, Vol. 126, No. 5–6, 2023, pp. 2037–2052.
- [47] Liu, S., K. Ding, H. H. Su, B. L. Zhuang, Q. L. Li, W. N. Lei, et al. A mathematical prediction model of the grinding force in ultrasonic-assisted grinding of ZrO₂ ceramics with experimental vali-

- dation. *Journal of Materials Engineering and Performance*, Vol. 2023, 2023, pp. 1–5.
- [48] Lu, M. M., Y. K. Yang, Y. H. Ma, J. Q. Lin, and Y. S. Du. Critical depth of cut modeling and ductility domain removal mechanism in elliptical vibration-assisted cutting BK7 optical glass. *The International Journal of Advanced Manufacturing Technology*, Vol. 2023, 2023, pp. 1–2.
- [49] Tang, J. Y., J. Du, and Y. P. Chen. Modeling and experimental study of grinding forces in surface grinding. *Journal of Materials Processing Technology*, Vol. 209, No. 6, 2009, pp. 2847–2854.
- [50] Li Y. Q. Study on surface quality of bearing raceway in ultrasonic vibration precision grinding with ceramic bonded CBN grinding wheel, Dissertation. Henan Polytechnic University, 2023.